



LUND UNIVERSITY

Phantom based qualitative and quantitative evaluation of artifacts in MR images of metallic hip prostheses.

Månsson, Sven; Müller, Gunilla; Wellman, Fredrik; Nittka, Mathias; Lundin, Björn

Published in:
Physica Medica

DOI:
[10.1016/j.ejmp.2014.12.001](https://doi.org/10.1016/j.ejmp.2014.12.001)

2015

[Link to publication](#)

Citation for published version (APA):
Månsson, S., Müller, G., Wellman, F., Nittka, M., & Lundin, B. (2015). Phantom based qualitative and quantitative evaluation of artifacts in MR images of metallic hip prostheses. *Physica Medica*, 31(2), 173-178. <https://doi.org/10.1016/j.ejmp.2014.12.001>

Total number of authors:
5

General rights

Unless other specific re-use rights are stated the following general rights apply:
Copyright and moral rights for the publications made accessible in the public portal are retained by the authors and/or other copyright owners and it is a condition of accessing publications that users recognise and abide by the legal requirements associated with these rights.

- Users may download and print one copy of any publication from the public portal for the purpose of private study or research.
- You may not further distribute the material or use it for any profit-making activity or commercial gain
- You may freely distribute the URL identifying the publication in the public portal

Read more about Creative commons licenses: <https://creativecommons.org/licenses/>

Take down policy

If you believe that this document breaches copyright please contact us providing details, and we will remove access to the work immediately and investigate your claim.

LUND UNIVERSITY

PO Box 117
221 00 Lund
+46 46-222 00 00

Phantom Based Qualitative and Quantitative Evaluation of Artifacts in MR Images of Metallic Hip Prostheses

Sven Månsson, PhD, Assoc. Prof.^{1*}, Gunilla M. Müller, MD², Fredrik Wellman, MSc¹,
Mathias Nittka, PhD³, Björn Lundin, PhD⁴

Affiliations

¹ Medical Radiation Physics, Dept. of Clinical Sciences Malmö,
Lund University, Skåne University Hospital Malmö, Sweden

² Radiology, Dept. of Clinical Sciences Malmö,
Lund University, Skåne University Hospital Malmö, Sweden

³ Siemens AG, Healthcare Sector, Imaging & Therapy Division,
Erlangen, Germany

⁴ Diagnostic Radiology, Dept. of Clinical Sciences Lund,
Lund University, Skåne University Hospital Lund, Sweden

* Corresponding author: Sven Månsson
Medical Radiation Physics Malmö
Skåne University Hospital
SE-205 02 Malmö
Sweden
Email: sven.mansson@med.lu.se

Running title: Evaluation of artifacts in MRI of metal prostheses

Abstract

Purpose

To develop methods for qualitative and quantitative evaluation of MRI artifacts near metallic prostheses, and to compare the efficiency of different artifact suppression techniques with different types of hip prostheses.

Methods

Three hip prostheses of cobalt-chromium, stainless steel, and titanium were embedded in agarose gel together with a rectilinear grid. Coronal MR images of the prostheses were acquired on a 1.5T scanner. Three pulse sequences were evaluated; TSE: a high-bandwidth turbo spin echo; VAT: TSE with view angle tilting, SEMAC: TSE with both VAT and slice distortion correction (6, 10 or 16 z -phase-encoding steps). Through-plane distortions were assessed as the length of visible gridlines, in-plane artifacts as the artifact area, and total artifacts by subtraction of an ideal, undistorted image from the actual image.

Results

VAT reduced in-plane artifacts by up to 50% compared to TSE, but did not reduce through-plane artifacts. SEMAC reduced through-plane artifacts by 60-80% compared to TSE and VAT. SEMAC in-plane artifacts were from 20% higher (6 encoding steps) to 50% lower (16 steps) than VAT. Total artifacts were reduced by 60-80% in the best sequence (SEMAC, 16 steps) compared to the worst (TSE). The titanium prosthesis produced 3-4 times lower artifact scores than the other prostheses.

Conclusions

A rectilinear grid phantom is useful for qualitative and quantitative evaluation of artifacts provoked by different MRI protocols and prosthesis models. VAT and SEMAC were supe-

rior to TSE with high bandwidth. A proper number of z -encoding steps in SEMAC was critical. The titanium prosthesis caused least artifacts.

Keywords

MR-imaging, artifacts, phantom studies, prostheses, musculoskeletal imaging

Introduction

After hip replacement with metallic implants several complications can arise, which eventually may lead to reoperation and exchange of the prosthesis [1, 2]. Magnetic resonance imaging (MRI) is normally well suited to detect the soft-tissue and skeletal abnormalities, but its diagnostic value can be hampered by artifacts caused by the metal. There is a variety of hip prostheses, from the classic Exeter or Charnley prosthesis with an articulation between polyethylene and cobalt-chrome or stainless steel, to newer materials such as titanium and the second-generation of metal-on-metal (MoM) hip prosthesis. The different materials and designs of the prostheses lead to different metal artifacts in MR examinations. Imaging protocols employing strong magnetic imaging gradients, achieved by high receiver bandwidth, RF pulses with high excitation bandwidth, thin slices, and high in-plane resolution, can improve the imaging quality near the prosthesis [3], but notwithstanding, substantial image distortions, signal voids, and signal pile-ups often persist. To obtain further artifact suppression the fundamental sequence design must be altered, and accordingly, several techniques with such aim have been developed; view angle tilting (VAT) [4, 5], slice encoding for metal artifact correction (SEMAC) [6], and Multi-Acquisition Variable-Resonance Image Combination (MAVRIC) [7]. VAT suppresses geometrical distortions within the imaging plane, whereas SEMAC and MAVRIC correct for the bending of the imaging plane near the metal.

However, while SEMAC and MAVRIC can achieve excellent artifact suppression, the scan time may easily be prolonged to an impractical level, depending on the severity of the magnetic field distortion caused by the implant [8]. To set up an imaging protocol with sufficient artifact suppression while maintaining a clinically acceptable scan time is a non-trivial task. Several studies have compared the performance of various sequences in patients with metallic prostheses [9, 10, 11], but while patient imaging is the ultimate test for

image quality, such attempts to evaluate artifacts (e.g. area or volume of artifacts) will depend on a more or less subjective evaluation conducted by a radiologist. More objective phantom-based methods can be useful for systematic comparison of different pulse sequences and for protocol optimization. Methods of varying complexity have been proposed, most of them measuring the total size of the artifact [12, 13, 14, 15]. Recently, Koff *et al.* proposed a method which separates through-plane and in-plane artifacts; however it was restricted to investigation of metallic objects of a fixed, cylindrical shape [16].

The purpose of the present study is to design phantom-based techniques for qualitative and quantitative evaluation of artifacts around prostheses of various shapes and materials, and to compare the efficiency of different artifact suppression techniques in imaging of three different types of hip prostheses.

Materials and Methods

Phantoms

Three phantoms were constructed, each one a container with a specific type of hip prosthesis embedded in agarose gel together with a 3-mm-thick rectilinear Perspex grid. The agarose gel was molded in two steps: first, the gel was allowed to harden after covering the lower half of the prosthesis, thereafter the grid was placed on the gel surface and more gel was added to fill the container (Fig. 1). The different prostheses were 1) BHR Cobalt-Chromium (Birmingham MoM hip resurfacing implant; Smith & Nephew Orthopaedics, Warwick, United Kingdom), 2) Stryker Exeter stainless steel, and 3) Stryker Omnifit Titanium + Cobalt-Chromium (Stryker Howmedica Osteonics, Allendale, NJ, USA). The Omnifit prosthesis had a titanium stem and a Cobalt-Chromium head. The material compositions are given in table 1.

MR-imaging

Phantom imaging was performed on a 1.5 T imager (MAGNETOM Avanto; Siemens Healthcare, Erlangen, Germany) using the spine matrix and body matrix coils. Three imaging sequences designed for suppression of metal artifacts were investigated: 1) turbo spin echo (TSE) with high readout bandwidth, 2) TSE with VAT, and 3) TSE with both VAT and SEMAC.

In the VAT sequence, the slice selection gradient is active not only during the play-out of the RF-pulses, but also during the signal acquisition. The additional magnetic field created by the slice gradient during the acquisition will counterbalance the geometric distortion along the readout direction caused by the distorted magnetic field around the metallic prosthesis (4, 5). The SEMAC technique uses a phase encoding gradient along the slice direction (the z -direction) similar to standard 3D sequences, but the field-of-view along the z -direction (governed by the number of z -phase encoding steps) is much larger than the thickness of the excited slices, thereby enabling tracking of the z -position of each slice. Data from all slices are then merged into a 3D volume, where signal missing from one slice due to slice bending is filled in from neighboring slices (6).

The VAT and VAT+SEMAC sequences were part of a works-in-progress package (WARP-WIP, Siemens AG). The SEMAC sequence was evaluated with 6, 10 and 16 z -phase encoding steps. Hereafter, the sequences are referred to as TSE, VAT, SEMAC 6, SEMAC 10, and SEMAC 16, respectively (table 2). All images were acquired in the coronal plane, with the middle section coinciding with the rectilinear grid.

Quantification of metal artifacts

Through-plane distortion bends the slices away from the plane of the grid, making the grid-lines disappear from areas where the through-plane distortion is severe. To quantify this distortion, the total length of “disappearing” grid lines was divided by the true total grid length:

$$Q_{\text{through-plane}} = \frac{\Sigma L_{\text{true}} - \Sigma L_{\text{visible}}}{\Sigma L_{\text{true}}}, \quad [1]$$

where ΣL denotes the total length of all vertical and horizontal grid lines.

To quantify in-plane artifacts, the artifact area was outlined by a region-of-interest (ROI) tool. To make this procedure operator-independent, intensity variations caused by non-uniform RF coil sensitivities were first equalized in Matlab (MathWorks, Natick, MA, USA) by fitting a 4th order polynomial surface to the pixels in the gel. Pixels with intensity values deviating substantially from the typical gel intensity (i.e. the metal artifacts) were excluded from the surface fit. A contour line corresponding to $\pm 30\%$ deviation from the equalized signal intensity was then overlaid on the MR image and served as a guide for the ROI drawing. The 30%-threshold was chosen, as it is the definition of metal artifact according to the ASTM standard [17]. The measured artifact area, A_{artifact} , thus comprises both artifacts and the signal void from the prosthesis itself. The true area of the prosthesis, $A_{\text{prosthesis}}$, was determined from a coronal X-ray projection matched to the MR image, because the contour of the prosthesis could not be determined reliably from the MR image (Fig. 2). As quantifier for the artifact size, we used

$$Q_{\text{in-plane}} = \frac{A_{\text{artifact}} - A_{\text{prosthesis}}}{A_{\text{prosthesis}}}. \quad [2]$$

A different approach was used to quantify both in-plane and through-plane artifacts in a single measure. An ideal, undistorted image of the phantom would only consist of two intensity levels: “black” in the grid, the prosthesis and the background air, and “white” in the gel. We denote this hypothetical image the “mask”. The mask was constructed from the X-ray projection and the least distorted (i.e. the SEMAC 16) MR image (Fig. 3). Artifacts in form of in-plane and through-plane distortions, signal voids and pile-ups, will all create deviations from the mask. In this approach, the artifact quantifier was defined as

$$Q_{total} = \frac{A_{pixel} \sum_{x,y} |I_{image}(x,y) - I_{mask}(x,y)|}{A_{prosthesis}}, \quad [3]$$

where A_{pixel} is the area of one pixel, and I_{image} and I_{mask} represent the pixel intensities of the MR image and the mask, respectively. Thus, one black pixel ($I = 0$) or two intermediately gray pixels ($I = 0.5$) in the image will both contribute with an artifact area in the nominator corresponding to one pixel, if the correct value should have been white ($I = 1$ in the mask). To reduce the influence from minor irrelevant intensity deviations due to noise or a non-perfect intensity equalization (i.e. the intensity in the gel is not perfectly flat), but which may persist over large areas, the summation in Eq. [3] was carried out only for pixels where $|I_{image} - I_{mask}| > T$. As for the artifact area measurement, the threshold T was chosen to 0.3, i.e. $\pm 30\%$.

For all artifact quantifiers, a lower value is better and an artifact-free image would get a score of zero.

Results

Qualitative findings

Images depicting the central slice through the grid are shown in Fig. 4 for all pulse sequences and prostheses. The x-ray contours of the prostheses are outlined in color. In-plane distortion (bent grid-lines in the readout direction; red arrow) is apparent in the TSE images, but barely noticeable in the VAT and SEMAC images. In the TSE and VAT images, through-plane distortion causes the gridlines to fade away near the prostheses (blue arrow), which is not discernible in the SEMAC images. The SEMAC images, on the other hand, exhibit sharp signal voids close to the prostheses (yellow arrows). These artifacts are more severe with lower number of z -encoding steps, but to some extent they persist even in the SEMAC 16-images. In SEMAC with large number of z -encoding steps, “zebra-patterns” of dark and bright lines appear at some locations (magenta arrow).

Quantification of through-plane distortion

The amount of missing gridlines was substantially lower in the SEMAC images than in the TSE and the VAT images, and decreasing with increasing number of z -encoding steps (Fig. 5). The VAT images obtained virtually identical artifact scores as the TSE images, which is reasonable since the VAT technique does not improve the slice profile. For all sequences, the artifact scores of the BHR MoM and the Exeter prostheses were similar, whereas the Omnifit prosthesis, made of titanium, resulted in a much smaller artifact score.

Quantification of in-plane distortion

The artifact area was substantially reduced in the VAT images compared to the TSE images, especially for the BHR MoM prosthesis where the artifact area was halved (Fig. 6). Additional improvement was obtained with the SEMAC sequences, given that the number of z -encoding steps was sufficiently large; 10 or 16. However, when the number of z -encoding

steps was too low, unresolved through-plane artifacts manifested themselves as dark regions, causing large artifact areas around the BHR MoM and Exeter prostheses with 6 z -encoding steps. These findings were also in agreement with the perceived image quality (Fig. 4). Again, the artifact area around the Omnifit prosthesis was much smaller compared to BHR MoM and Exeter.

Total artifact quantification

Images of the metal artifacts, i.e. the magnitude of the difference between the image and the mask, are depicted in Fig. 7. It is apparent that the slices of the TSE and VAT images are bent, because the artifact intensity is high at the gridlines near the prostheses. The SEMAC images do not have artifacts along the gridlines, indicating that the slices are correctly positioned, but instead have large artifact bumps which reduce in size with increasing numbers of z -encoding steps. The total artifact score was accordingly lowest for the SEMAC 16 images, but even the SEMAC 6 images had a better score than the VAT images (Fig. 8). Again, the artifact scores were by far lowest for the Omnifit prosthesis.

Discussion

We describe phantom-based methods for quantitative analyses of various artifacts arising in the surrounding of metallic prostheses which enable objective comparison of different imaging techniques and orthopedic implants. In contrast to previously reported phantom studies which have aimed at quantifying the artifact size only, the methods proposed here in addition give information of how well the artifacts are suppressed both in-plane and through-plane. These two quantities are not necessarily linked; for example, the TSE and VAT sequences were equivalent with respect to through-plane artifacts, but the VAT sequence was superior regarding in-plane artifacts.

The results for the SEMAC sequence highlight the importance of finding a proper value for the number of z -encoding steps; since the scan time scales in proportion to this parameter, it should not be set higher than necessary, but a too low value may create severe artifacts and render the scan diagnostically useless (Fig. 4). Regarding the quantitative artifact measures, the rank order (worst to best) of the sequences was $TSE \rightarrow VAT \rightarrow SEMAC$, and the Omnifit titanium prosthesis created considerably less artifacts than the BHR MoM cobalt-chromium and the Exeter stainless-steel prostheses due to the lower magnetic susceptibility of titanium. These experiences are in agreement with the results of other studies comparing artifacts provoked by titanium, stainless steel, and cobalt-chromium prostheses when using TSE, VAT and SEMAC/MAVRIC pulse sequences [13, 15, 16]. Moreover, it is apparent from the images in Fig. 4, that much information about the severity and nature of the artifacts can be deduced just from a visual inspection of the rectilinear grid, without a formal mathematical quantification. Accordingly, phantoms of this kind can also be expedient for more convenient protocol optimization at radiology departments with a multitude of sequence variants for metal artifact reduction.

A limitation of the present study was that only the artifacts in a single, central slice were analyzed. The SEMAC technique depends on that signal missing in a slice can be filled in from neighboring slices. If the artifact volume is not fully covered by the slice package, the artifact suppression in slices near the edges of the package will thus be less perfect than in the central slice. The effect of the number of slices in the SEMAC acquisition would therefore also have been of interest to investigate, but notwithstanding, we believe the image of the central slice through the prosthesis provides a representation of sufficient relevance for most purposes. In theory, the artifact area measurement could be supplemented by a 3D volume measurement, albeit being more cumbersome and without normalization to the true prosthesis dimensions. Another limitation of the total artifact quantification was that the

mask image was not a completely perfect construction. It is difficult to find materials which are X-ray dense while generating absolutely no artifacts in MR imaging, and we used the best available MR image. A more laborious alternative could be to use a digital photo of the grid and the prosthesis before completing the agarose gel molding. It is also important to note that the evaluation methods used in the study cannot fully distinguish through-plane from in-plane artifacts for the SEMAC technique. As apparent in Fig. 6, an insufficient number of z -encoding steps give rise to large artifact areas in the SEMAC 6 images, although they originate from a through-plane rather than an in-plane phenomenon. Nevertheless, the artifact area reflects the perceived image quality (Fig. 4).

In summary, we present a technique for evaluation of artifacts around metallic implants. By the use of a rectilinear grid phantom, images suited for both qualitative and quantitative evaluation of MRI protocols and prosthesis models are produced. The benefits of the VAT and SEMAC techniques over standard TSE protocols, even if optimized with high receiver bandwidth, were demonstrated. For the SEMAC-sequence it is crucial that the number of SEMAC z -encoding steps is sufficiently high to avoid artifacts, this depending on the severity of the field distortion created by the prosthesis. The prosthesis material titanium caused substantially less artifacts than cobalt-chromium or stainless steel.

Acknowledgements

The authors thank Johan Olsrud, PhD, Lund University, and Jonas Svensson, PhD, Lund University, for valuable suggestions.

References

1. Dorr LD, Wan Z, Longjohn DB, Dubois B, Murken R. Total hip arthroplasty with use of the Metasul metal-on-metal articulation. Four to seven-year results. *J Bone Jt Surg Am* 2000;82(6):789-98.
2. Bjorgul K, Novicoff WN, Andersen ST, et al. High rate of revision and a high incidence of radiolucent lines around Metasul metal-on-metal total hip replacements: results from a randomised controlled trial of three bearings after seven years. *Bone Jt J* 2013;95-B(7):881-6.
3. Vandevenne JE, Vanhoenacker FM, Parizel PM, Butts Pauly K, Lang RK. Reduction of metal artefacts in musculoskeletal MR imaging. *JBR e BTR* 2007;90(5):345-9.
4. Cho ZH, Kim DJ, Kim YK. Total inhomogeneity correction including chemical shifts and susceptibility by view angle tilting. *Med Phys* 1988;15(1):7-11.
5. Olsen RV, Munk PL, Lee MJ, et al. Metal artifact reduction sequence: early clinical applications. *Radiographics* 2000;20(3):699-712.
6. Lu W, Pauly KB, Gold GE, Pauly JM, Hargreaves BA. SEMAC: slice encoding for metal artifact correction in MRI. *Magn Reson Med* 2009;62(1):66-76.
7. Koch KM, Lorbiecki JE, Hinks RS, King KF. A multispectral three-dimensional acquisition technique for imaging near metal implants. *Magn Reson Med* 2009;61(2):381-90.

8. Hargreaves BA, Chen W, Lu W, et al. Accelerated slice encoding for metal artifact correction. *J Magn Reson Imaging* 2010;31(4):987-96.
9. Chen CA, Chen W, Goodman SB, et al. New MR imaging methods for metallic implants in the knee: artifact correction and clinical impact. *J Magn Reson Imaging* 2011;33(5):1121-7.
10. Hayter CL, Koff MF, Shah P, Koch KM, Miller TT, Potter HG. MRI after arthroplasty: comparison of MAVRIC and conventional fast spin-echo techniques. *AJR - Am J Roentgenol* 2011;197(3):W405-11.
11. Sutter R, Ulbrich EJ, Jellus V, Nittka M, Pfirrmann CW. Reduction of metal artifacts in patients with total hip arthroplasty with slice-encoding metal artifact correction and view-angle tilting MR imaging. *Radiology* 2012;265(1): 204-14.
12. Lee MJ, Janzen DL, Munk PL, MacKay A, Xiang QS, McGowen A. Quantitative assessment of an MR technique for reducing metal artifact: application to spin-echo imaging in a phantom. *Skelet Radiol* 2001;30(7):398-401.
13. Kolind SH, MacKay AL, Munk PL, Xiang QS. Quantitative evaluation of metal artifact reduction techniques. *J Magn Reson Imaging* 2004;20(3):487-95.
14. Olsrud J, Latt J, Brockstedt S, Romner B, Bjorkman-Burtscher IM. Magnetic resonance imaging artifacts caused by aneurysm clips and shunt valves: dependence on field strength (1.5 and 3 T) and imaging parameters. *J Magn Reson Imaging* 2005;22(3):433-7.

15. Ai T, Padua A, Goerner F, Nittka M, Gugala Z, Jadhav S, et al. SEMAC-VAT and MSVAT-SPACE sequence strategies for metal artifact reduction in 1.5T magnetic resonance imaging. *Invest Radiol* 2012;47(5):267-76.
16. Koff MF, Shah P, Koch KM, Potter HG. Quantifying image distortion of orthopedic materials in magnetic resonance imaging. *J Magn Reson Imaging* 2013;38(3):610-8.
17. American Society for Testing and Materials (ASTM). 21199-F2207. Standard test method for evaluation of MR image artifacts from passive implants. West Conshohocken, PA: ASTM International; 2007. p. 1-4.

Figure captions

Figure 1.

Construction of the prosthesis phantom (Omnifit), showing the prosthesis surrounded by the rectilinear Perspex grid. The agarose gel to fill the upper half of the container is not yet added (A). The schematic drawing shows the prosthesis and the grid from a lateral view (B).

Figure 2.

X-ray (left) and MR image (right) of the Exeter prosthesis, showing the mid slice aligned with the rectilinear grid. The blue line is the contour of the prosthesis, as determined from the X-ray projection. Note that the contour cannot be determined from the MR image.

Figure 3.

The process of quantifying total artifacts caused by both in-plane and through-plane effects combined, shown for the Exeter prosthesis. An ideal, undistorted mask is created from the X-ray projection and the best MR image (SEMAC 16). The parts of the grid that were obscured by remaining artifacts were filled out by hand. Smooth intensity variations due to varying sensitivity of the RF-coils are equalized with a 4th order polynomial surface before the difference is taken between the mask and the image under evaluation.

Figure 4.

MR images depicting the central slice of all prostheses and imaging sequences. The yellow lines represent the X-ray contours of the prostheses. Red arrow = in-plane bending of grid line, blue arrow = fading of grid line due to through-plane distortion, yellow arrows = sharp signal voids, magenta arrow = “zebra-pattern” artifacts in SEMAC images.

Figure 5.

Through-plane image distortion, expressed as the missing grid length ($= \text{true grid length} - \text{visible grid length}$) divided by the true grid length. The grid length was obtained by adding the lengths of all horizontal and vertical lines. Equal distortions are seen for the TSE and VAT images, while the SEMAC images correct most of the distortion.

Figure 6.

In-plane distortion, quantified by the $(\text{artifact area} - \text{true prosthesis area})$ divided by the true prosthesis area. The distortion is much improved in the VAT images compared to the TSE images. The SEMAC images are more artifact-free than the VAT images, but for the BHR Mom and Exeter prostheses only if the number of z -encoding steps is sufficiently large.

Figure 7.

Images showing the absolute difference $|\text{Image} - \text{Mask}|$, which represents the magnitude of the metal artifacts. Bright signal along the gridlines indicate strong through-plane distortion, clearly seen in the TSE and VAT images. Only pixel values >0.3 were included when calculating the total artifact measure shown in Fig. 8.

Figure 8.

Total artifact measure for the five investigated imaging sequences and three prostheses. The total artifact was calculated by adding the pixel values of all pixels with intensity >0.3 in Fig. 7, and multiplying with the ratio between the pixel area and the prosthesis area.

Figure 1

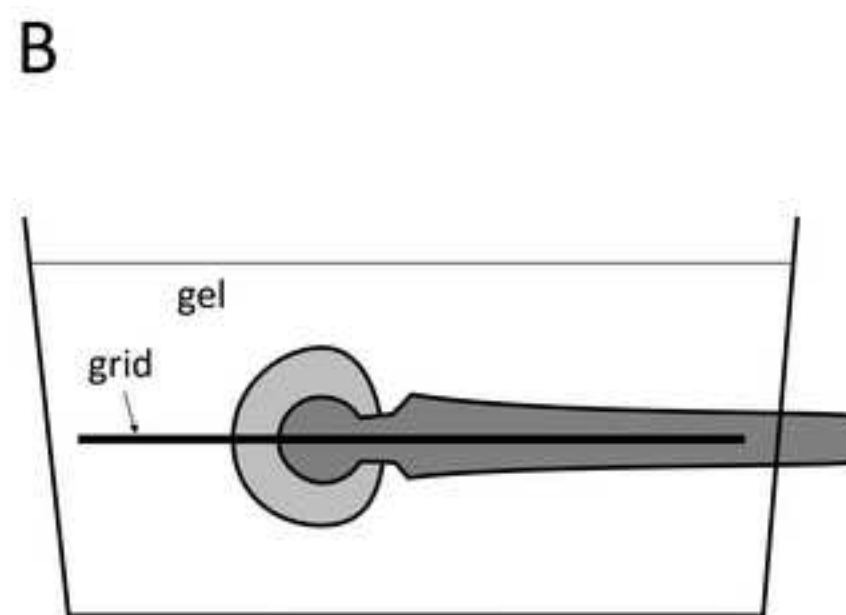


Figure 2

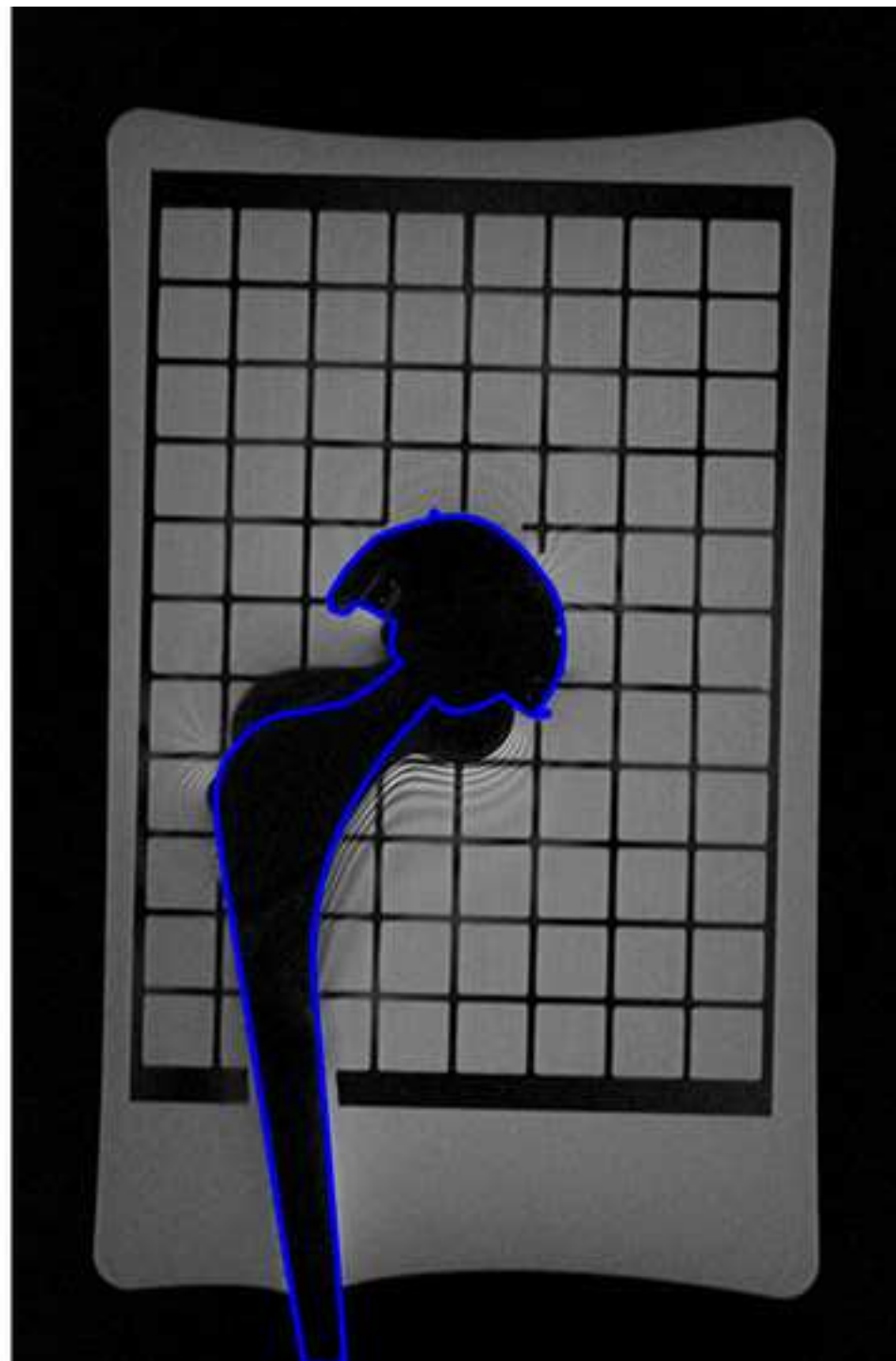


Figure 3

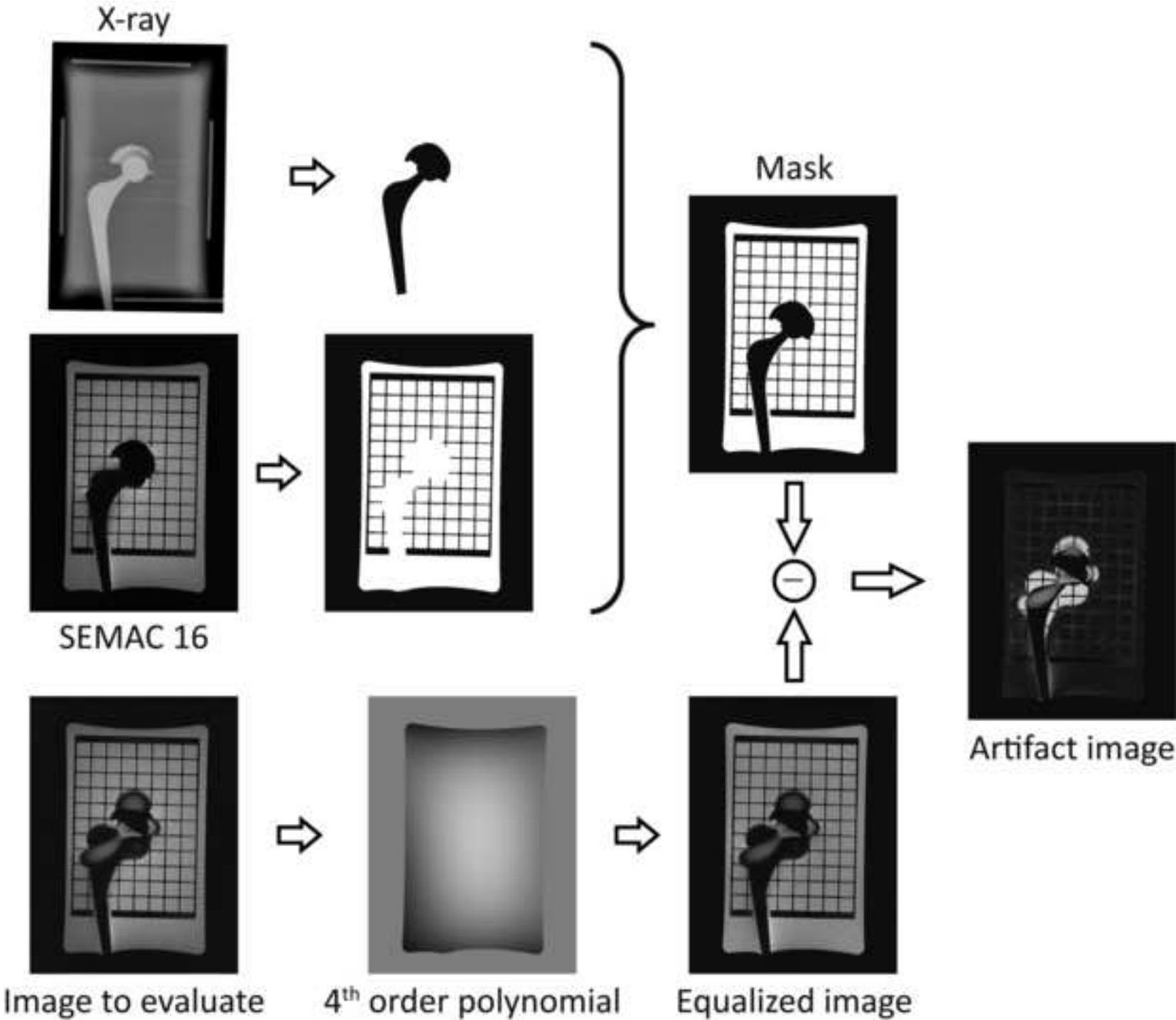


Figure 4

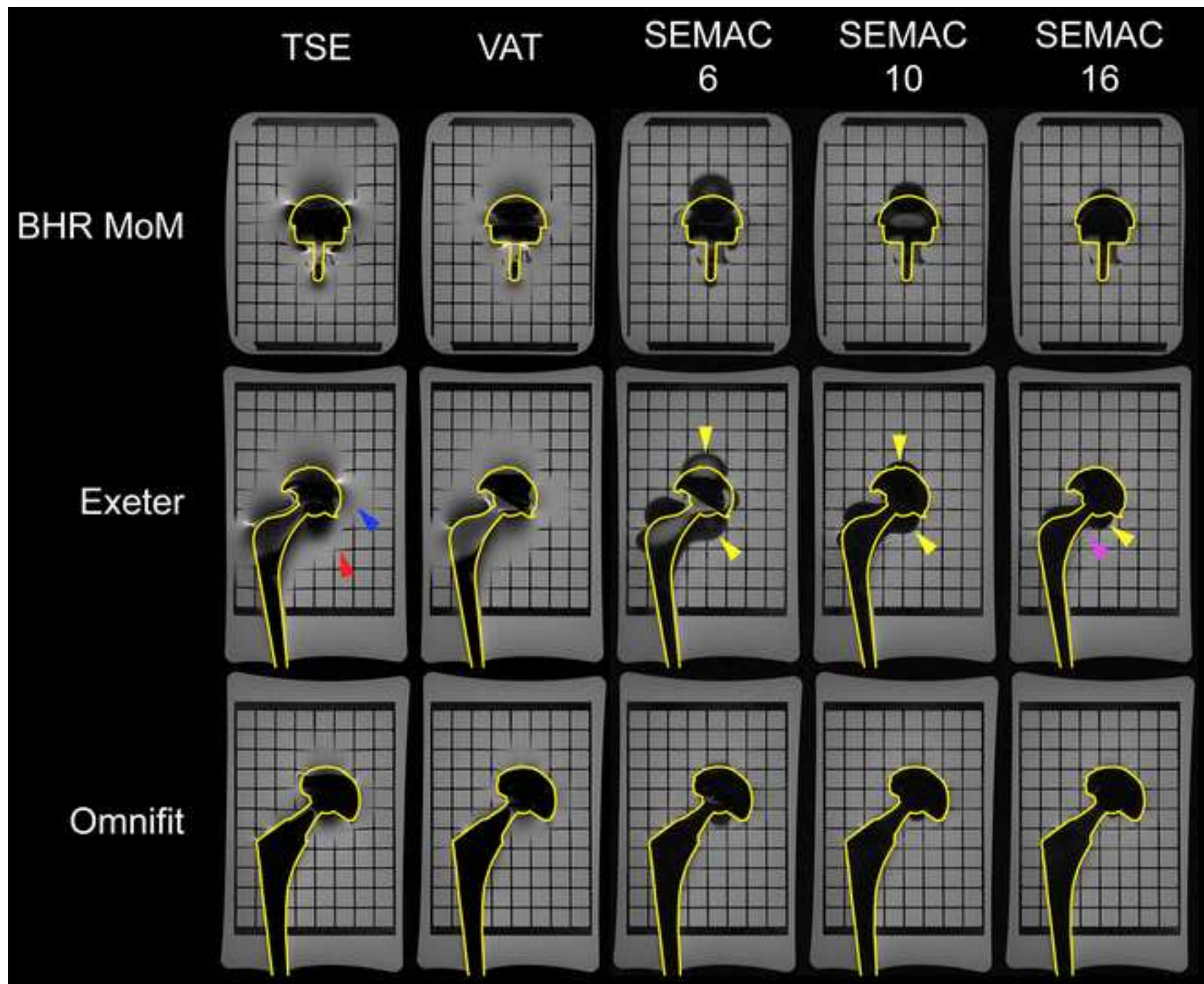


Figure 5

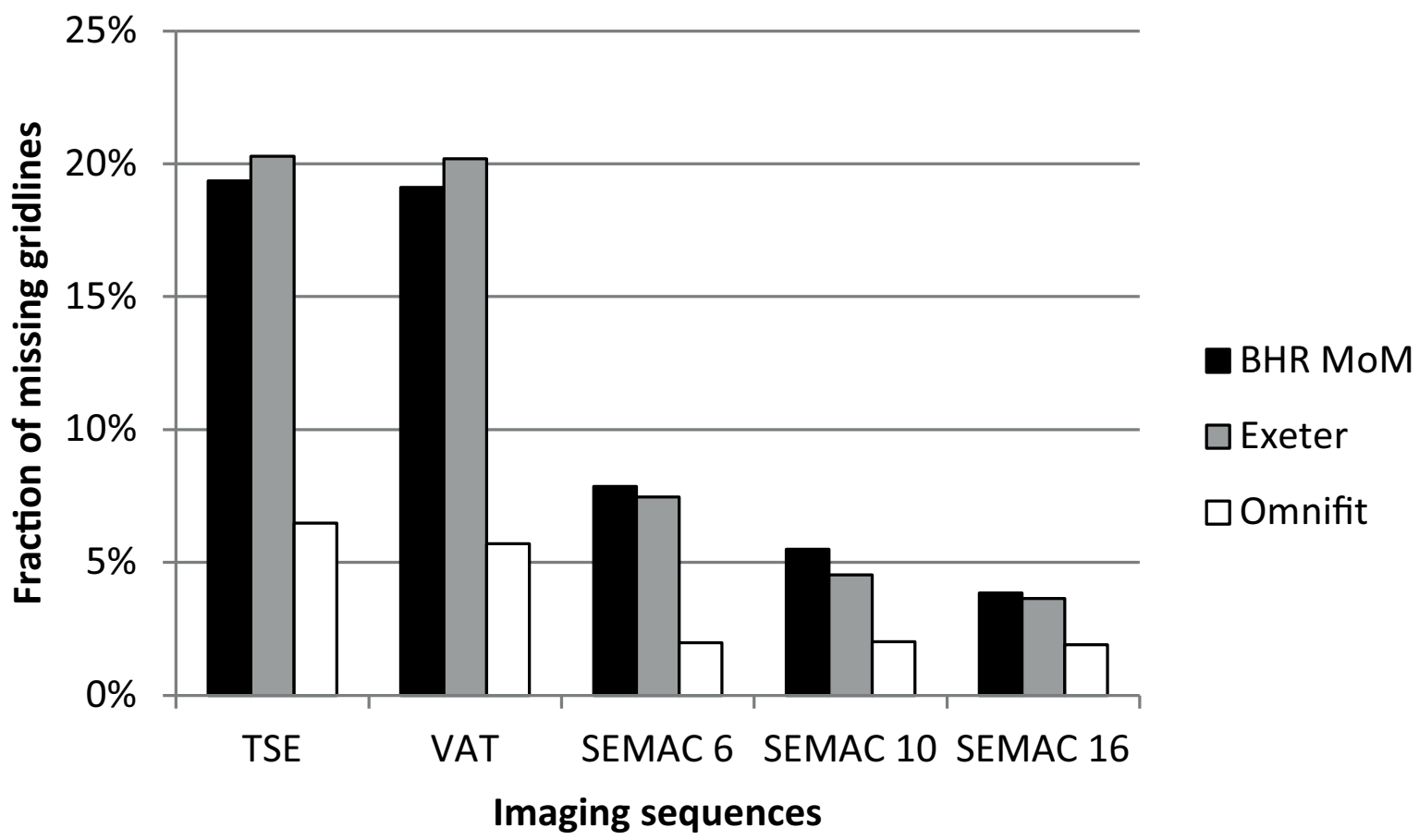


Figure 6

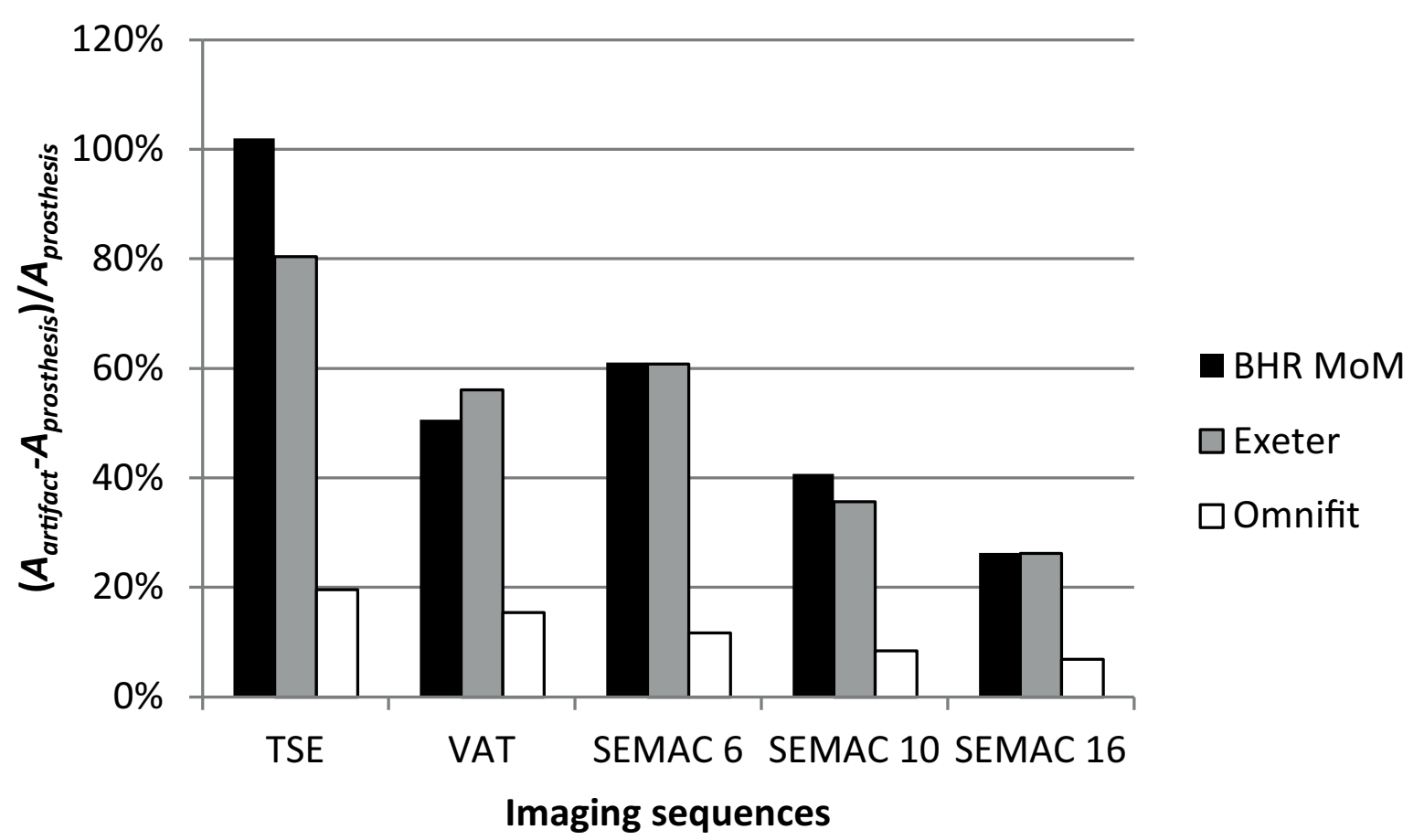


Figure 7

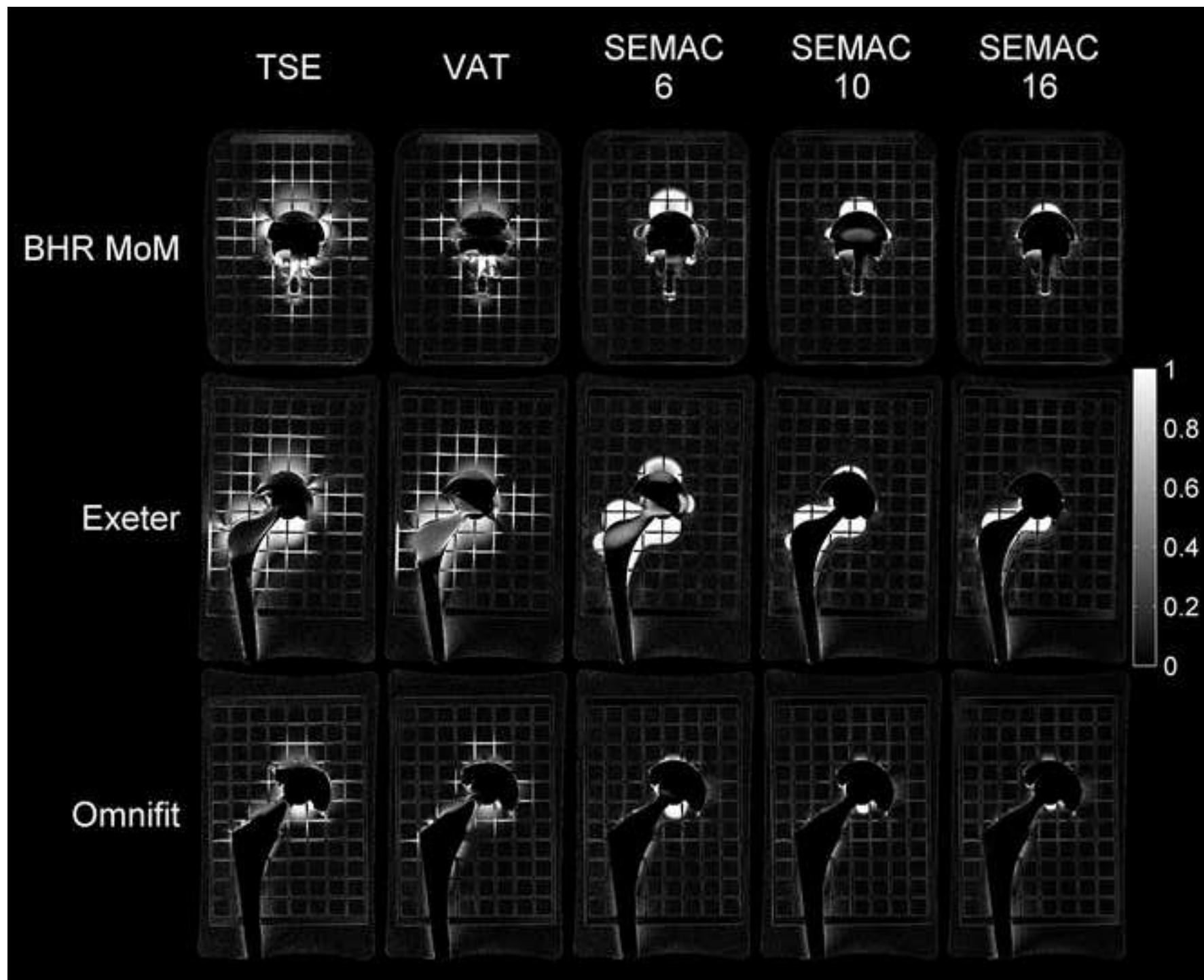


Figure 8

